Contrib Mineral Petrol (2012) 164:245–259
DOI 10.1007/s00410-012-0736-6

ORIGINAL PAPER

# Low-temperature zircon growth related to hydrothermal alteration of siderite concretions in Mississippian shales, Scotland

**Maciej J. Bojanowski · Bogusław Bagiński · Euan Clarkson · Ray Macdonald · Leszek Marynowski**

Received: 1 August 2011 / Accepted: 3 March 2012 / Published online: 21 March 2012


**Abstract** Zircon occurs in voids and cracks in phosphatic coprolites enclosed in siderite concretions in Mississippian shales near Edinburgh, Scotland. The zircon formed during hydrothermal alteration of early-diagenetic concretions and occurs as spherical aggregates of prismatic crystals, sometimes radiating. Vitrinite reflectance measurements indicate temperatures of ~270°C for the zircon-bearing concretions and the host shales. Molecular parameter values based on dibenzothiophene and phenanthrene distribution and occurrence of di- and tetra-hydro-products of polycyclic aromatic compounds suggest that the rocks experienced relatively high-temperature aqueous conditions related to hydrothermal fluids, perhaps associated with neighboring mafic intrusions. The zircon was dissolved from the concretions, transported in fluids, and reprecipitated in voids. This is the first record of the precipitation of authigenic zircon in sedimentary rock as a new phase, not as outgrowths.

Communicated by H. Keppler.

**Electronic supplementary material** The online version of this article (doi:10.1007/s00410-012-0736-6) contains supplementary material, which is available to authorized users.

M. J. Bojanowski (✉) · B. Bagiński · R. Macdonald
Institute of Geochemistry, Mineralogy and Petrology, University of Warsaw, Żwirki i Wigury 93, 02-089 Warsaw, Poland
e-mail: mcbojan@uw.edu.pl

E. Clarkson
School of Geosciences, University of Edinburgh, West Mains Road, EH9 3JW Edinburgh, UK

L. Marynowski
Faculty of Earth Sciences, University of Silesia, Będzińska 60, 41-200 Sosnowiec, Poland

**Keywords** Zircon · Concretions · Diagenesis · Hydrothermal alteration · Vitrinite reflectance · PAHs

## Introduction

Zircon can crystallize under pressure (*P*)–temperature (*T*) conditions ranging from those in the mantle to the low *P* and *T* pertaining to diagenesis. Low-temperature zircon growth, including examples from sedimentary environments, has been well documented in the literature (Geisler et al. 2003; Rasmussen 2005; Hay and Dempster 2009; Hay et al. 2010). Rasmussen (2005) reported minute (typically <3 μm) zircon outgrowths on detrital grains from several low-grade metasedimentary sequences, especially shales, and related its growth to the transport of Zr in aqueous fluids, possibly as F complexes, during very low-grade metamorphism. Using zircons from Carboniferous sandstones in Scotland, Hay and Dempster (2009) showed that metamict zircon alters to low-temperature zircon in sedimentary rocks at temperatures <100 °C. The new zircon takes two forms: nano-crystalline zircon, formed by a dissolution–reprecipitation process, and microcrystalline zircon, formed via diffusion-driven transformation. Growth of both forms was promoted by the presence of hydrous fluids. Hay et al. (2010) described low-temperature zircon outgrowths on detrital zircon in a greenschist facies slate from the Scottish Highlands, the outgrowths preserving a complex polyphase growth history during cooling and exhumation.

Here, we report on what we believe to be a unique occurrence of zircon, as veins in siderite concretions. We attempt, via a multidisciplinary study, to understand the way in which the composition and structure of the zircon reflect the unusual paragenesis and to determine the

conditions under which zircon was formed, especially temperature. We understand that this is the first report on precipitation of authigenic zircon in sedimentary rocks as a new phase, not as outgrowths.

Zircon was identified by scanning electron microscopy (SEM), and more detailed imaging was done by field emission SEM (FE-SEM). The chemical composition was determined by electron microprobe analysis (EMPA). Stable C and O isotopes were used to assess the genesis of the concretions, particularly the timing of their formation and the source of fluids. The content and nature of carbonates in the cements were estimated by thermal analysis. Biomarker analysis was employed to determine the thermal maturity and sources of the organic matter. Maximum temperatures of diagenesis were estimated by vitrinite reflectance.

## Geological background and description of material

Along Edinburgh's shore (Scotland) (Fig. 1a), Mississippian sedimentary rocks (shales and sandstones) are interbedded with basaltic lava flows and tuffs. This volcano-sedimentary sequence is locally intruded by mafic sills of Pennsylvanian through lower Permian age (Fig. 1b). The largest are more than a 100 m thick, but in the vicinity of the studied outcrops, they occur as sheets about 1 m thick. Throughout the Carboniferous in the Midland Valley of Scotland, there was a more or less continuous extrusive and intrusive igneous activity. The Arthur's Seat volcanic complex was active from the early Visean onwards, some sills and dykes were intruded at about the same time, and the eastern Midland Valley was the site of emplacement of many other intrusions that continued through the Carboniferous. Figure 1b shows large numbers of sills, many of which are connected at different levels within the sedimentary rocks; dykes are omitted for clarity. The important point here is that the sediments must have been heated for a long time as a result of all this activity.

The samples come from Wardie, east of Granton Harbour, from an extensive outcrop of rocks (Fig. 1c), known as the Wardie Shales. These rocks, visible only at low tide, are some 65 m thick and lie within the Holkerian to Asbian Lower Oil Shale Group. The succession at Wardie consists largely of black organic-rich shales with ironstone concretions. The concretions are numerous and dispersed randomly within unfossiliferous and fish-bearing varieties of the shales (Fig. 1c). The Wardie Shales are covered by at least 700 m of sedimentary rocks higher in the Carboniferous. However, they were buried deeply enough to have reached the oil window in the Early Permian (George 1990, 1993) and therefore at depths far greater than 700 m.

The main interest of this succession has been palaeontological, for the concretions are the source of many superbly preserved fossil fish, chiefly palaeoniscids, described by Ramsay Traquair between 1877 and 1914. Although great numbers of fish-bearing concretions have been collected over the years and are stored mainly in the National Museums of Scotland, Edinburgh, the great majority of the concretions contain only spiral coprolites. These may either be faecal, or the preserved and altered contents of a decayed spiral fish intestine (Sumner 1991). The succession is summarized by Wood (1975) and Clarkson (1986). These beds are largely non-marine and

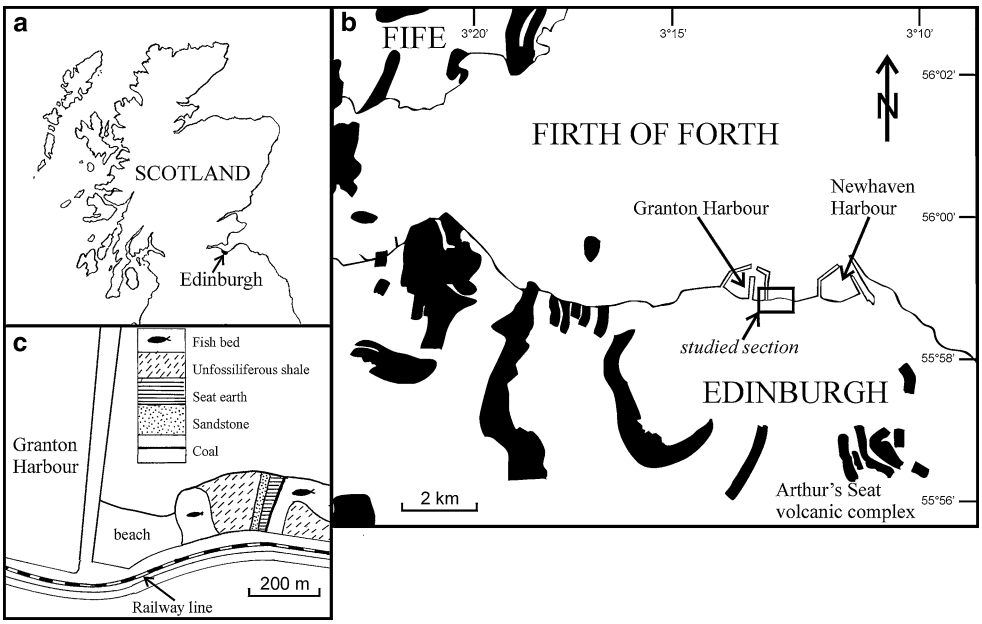


**Fig. 1** Location maps. **a** Location of Edinburgh. **b** Distribution of Carboniferous sills (*black areas*) in the vicinity of Edinburgh (based on the online geological map viewer from British Geological Survey website: http://maps.bgs.ac.uk/geologyviewer); dykes and extrusive igneous rocks are omitted for clarity. **c** Location and lithologies of the Wardie Shales in the outcrop studied. Samples were collected from unfossiliferous and fish-bearing varieties of the shales. The *blank area* south of the outcrop is unexposed ground

were apparently deposited in a large brackish or freshwater basin (Read et al. 2002). Sixteen random concretions (A to P) and 6 shale specimens (As1 to Ms) from the host material immediately surrounding the concretions have been examined.

## Methods

Standard petrographic microscopy was performed on thin sections. Because the rocks examined are very fine-grained, detailed observations and analyses of mineral composition were made by electron microscopy. Uncovered thin sections, polished and coated with carbon, were examined using a WDS Cameca SX-100 microprobe (Faculty of Geology, University of Warsaw). Observations were made using back-scattered electron (BSE) imaging. Operating conditions were as follows: 15 kV accelerating potential, 10–20 nA beam current. The following standards were used: REE phosphates for selected REE (Gd, Nd, Sm, Pr, Ce) and glasses containing defined contents of REE (Yb, Tm, Er, Ho, Dy); La—$LaB_6$; Si and Zr—natural zircon; Hf—Hf spinel; Y—YAG; Ti—natural rutile; and P—natural apatite. Uncoated thin sections, and rock chips coated with gold were examined using a JEOL JSM-6380LA scanning electron microscope equipped with EDS analyzer (Faculty of Geology, University of Warsaw). Observations on BSE were carried out on thin sections, while secondary electron (SE) imaging was performed on rock chips. Field Emission FEI Nova NanoSEM 200 equipment (Institute of Ceramics and Building Materials, Warsaw) was used for detailed SE imaging of the investigated phases. Operating conditions were as follows: 10 kV accelerating potential and TLD detector. Samples were sputtered with gold. Thermal differential analyses on powdered samples of concretions (A, B, and I) and shales (As1 and Bs1) were carried out with a Derivatograph MOM Q-1500D. Analysis parameters were as follows: sample starting net weight—400 mg, sensitivity—200 mg, corundum crucibles, and heating rate—10°/min.

Stable carbon and oxygen isotope measurements were taken on 36 powdered bulk samples (from 14 concretions) reacted with 100 % phosphoric acid (density >1.9, Wachter and Hayes 1985) at 75°C using a Kiel III online carbonate preparation line connected to a ThermoFinnigan 252 mass spectrometer (University of Erlangen-Nürnberg, Germany). All values are reported in per mil relative to V–PDB by assigning a $\delta^{13}C$ value of +1.95‰ and a $\delta^{18}O$ value of −2.20‰ to NBS19. Reproducibility ($1\sigma$) was verified by replicate analyses of laboratory standards and is better than ±0.02‰ for $\delta^{13}C$ and ±0.03‰ for $\delta^{18}O$. Oxygen isotopic compositions were corrected using the fractionation factor between siderite- and phosphoric acid-extracted $CO_2$ given by Rosenbaum and Sheppard (1986). Samples were collected using sintered diamond microdrills (diameter 2 or 3 mm). Major and trace element whole-rock analyses were carried out by inductively coupled plasma mass spectroscopy (ICP-MS) at AcmeLabs, Vancouver, Canada. Details of analytical methods can be found at the website http://acmelab.com.

For vitrinite reflectance analysis, freshly polished rock fragments were used. Random reflectance was measured in samples As2, Bs1, M, and Ms using an AXIOPLAN II microscope using 546 nm light and oil of 1.546 RI using a total magnification of 500X. The standards used were 0.898, 1.42, and 1.71 % reflectance ($R_o$).

The GC–MS analyses were performed on samples A, As1, B, Bs1, C, and D with an Agilent 6890 Series Gas Chromatograph interfaced to an Agilent 5973 Network Mass Selective Detector and Agilent 7683 Series Injector (Agilent Technologies, Palo Alto, CA). A 0.5 µL sample was introduced into the cool on-column injector under electronic pressure control. Helium (6.0 Grade, Linde, Kraków) was used as the carrier gas at a constant flow rate of 2.6 mL/min. The GC separation was carried out on one of the two following fused-silica capillary columns:

1. J&W HP5-MS (60 m × 0.32 mm i.d., 0.25 µm film thickness) coated with a chemically bonded phase (95 % polydimethylsiloxane, 5 % diphenylsiloxane). The GC oven temperature was programmed for heating from 40 °C (isothermal for 1 min) to 120 °C at a rate of 20 °C/min and then to 300 °C at a rate of 3 °C/min. The final temperature was held for 35 min.
2. J&W DB35-MS (60 m × 0.25 mm i.d., 0.25 µm film thickness) coated with a chemically bonded phase (35 % phenyl-methylpolysiloxane). The GC oven temperature was programmed from 50 °C (isothermal for 1 min) to 120 °C at a rate of 20 °C/min and then to 300 °C at a rate of 3 °C/min. The final temperature was held for 45 min. More details about organic matter separation, GC–MS conditions, and organic compounds identification have been published by Marynowski et al. (2011).

## Results

### Petrography

The shales from Wardie are fine-grained clastics deposited in a large brackish or freshwater basin (Read et al. 2002). They are rich in organic matter, mainly plant remains. They also contain biogenic phosphates (fish remains). The siliciclastic material is mainly aleuritic and comprises quartz, potassium feldspar, plagioclase, lithic fragments,

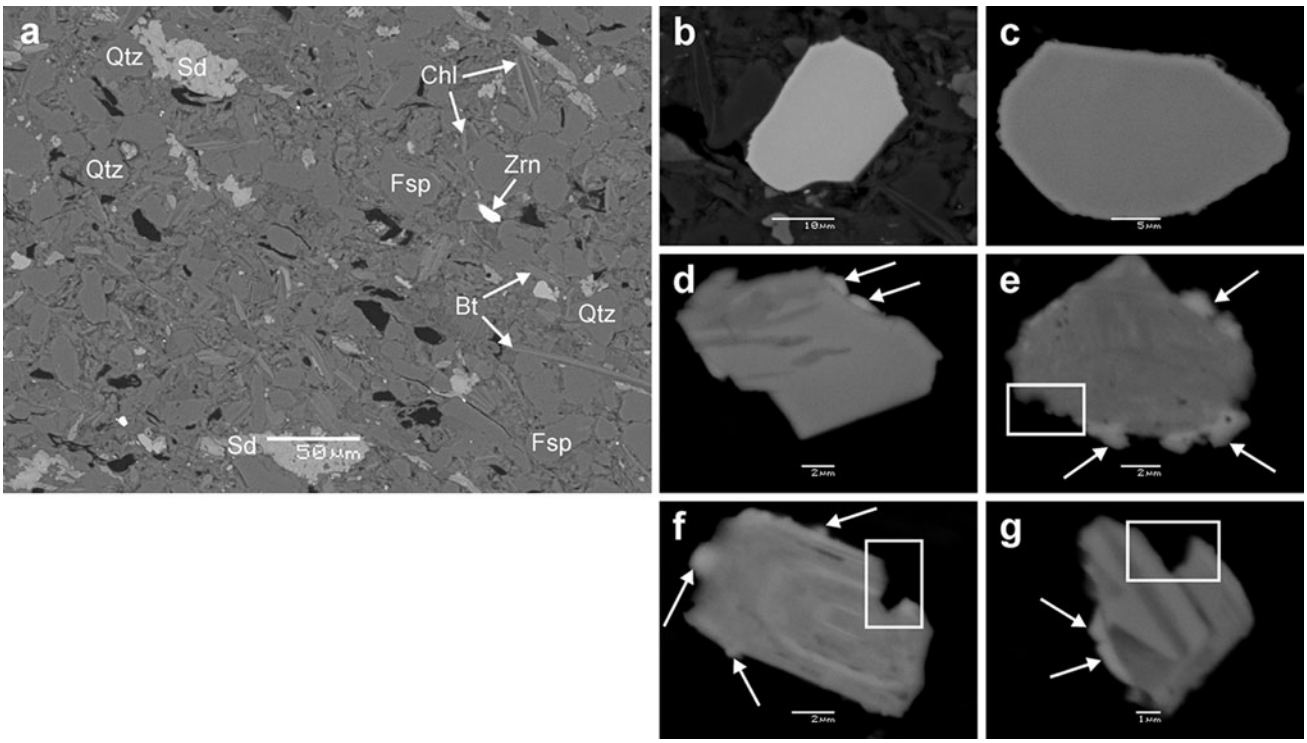


**Fig. 2** Scanning electron images (BSE) of the shales. **a** Sample As1. *Black grains* are coal, *large isometric dark gray grains* are quartz (Qtz) or feldspars (Fsp), platy minerals are biotite (Bt, *dark gray*) and chlorite (Chl, *light gray*), *very light gray* is Mg-rich siderite (Sd) in nests, and *white* is detrital zircon (Zrn). **b–g** Zircon grains from the shales (**b–d** sample As1, **e–g** sample As2). Embayments probably caused by corrosion are marked in the *rectangles*. *Arrows* indicate overgrowths of an unidentified phase (brighter in BSE) on zircon grains

biotite, chlorite, mixed-layer clay minerals, and heavy minerals, including xenotime, allanite, monazite, and zircon (Fig. 2a). The largest zircon grains attain 30 µm, but they are usually about 10 µm. Zircon is evidently detrital, as it occurs between other grains and is usually rounded (Fig. 2b, c). Some zircon grains exhibit complex outlines (Fig. 2e–g). Others are overgrown by an authigenic phase, which is brighter in BSE (Fig. 2d–g). Among authigenic phases, pyrite (mostly framboidal), siderite (Fig. 2a), and ankerite are early-diagenetic and kaolinite and quartz late-diagenetic.

The concretions have typical ellipsoidal shapes (Fig. 3a) and reach 40 cm in diameter. The laminae of the host shales are warped around them. The internal structure of the concretions is usually homogenous; only some of them show concentric zoning. All specimens envelope fossils. The great majority contain spiral coprolites composed of amorphous Ca-phosphate and organic matter (Fig. 3). Others contain fish or plant remains.

The concretions were formed by the precipitation of Fe-rich minerals, mostly siderite, but ankerite and pyrite are also abundant (Fig. 3a, d). Microprobe and EDS analyses revealed that the carbonates have very variable composition. Generally, Mg-rich siderite and Ca-rich ankerite are the predominant phases, while calcite is rather rare (Fig. 3d). Thermal differential analysis revealed that some of the concretions contain similar quantities of siderite and ankerite, but most are sideritic with only a few per cent of other carbonates, indistinguishable at such low concentrations. Generally, the concretions contain from 70 up to 86 % of carbonate minerals.

These concretionary phases cemented the material of the host sediments, so that all the detrital and biogenic materials in the shales are enclosed within the concretions, although dispersed among the concretionary cements. The only difference is that detrital heavy minerals (xenotime, allanite, monazite, and zircon) are extremely rarely found (Supplementary Figure 1), despite careful and systematic search performed on thin sections using SEM (BSE imaging). A standard thin section usually hosts no more than several zircon grains a few micrometer large (Supplementary Figure 1a), sometimes even none. Various late authigenic phases appear within the residual porosity and septarian cracks (Figs. 3, 4, 5, 6): kaolinite, pyrite, and calcite are the most abundant, whereas quartz, chlorites, ankerite, siderite, baryte, galena, chalcopyrite, and wurtzite are less frequent. It is important to note that authigenic euhedral F-rich apatite is also found there (Fig. 3c; Supplementary Table 1). These minerals have been identified by means of petrographic microscopy and/or SEM.

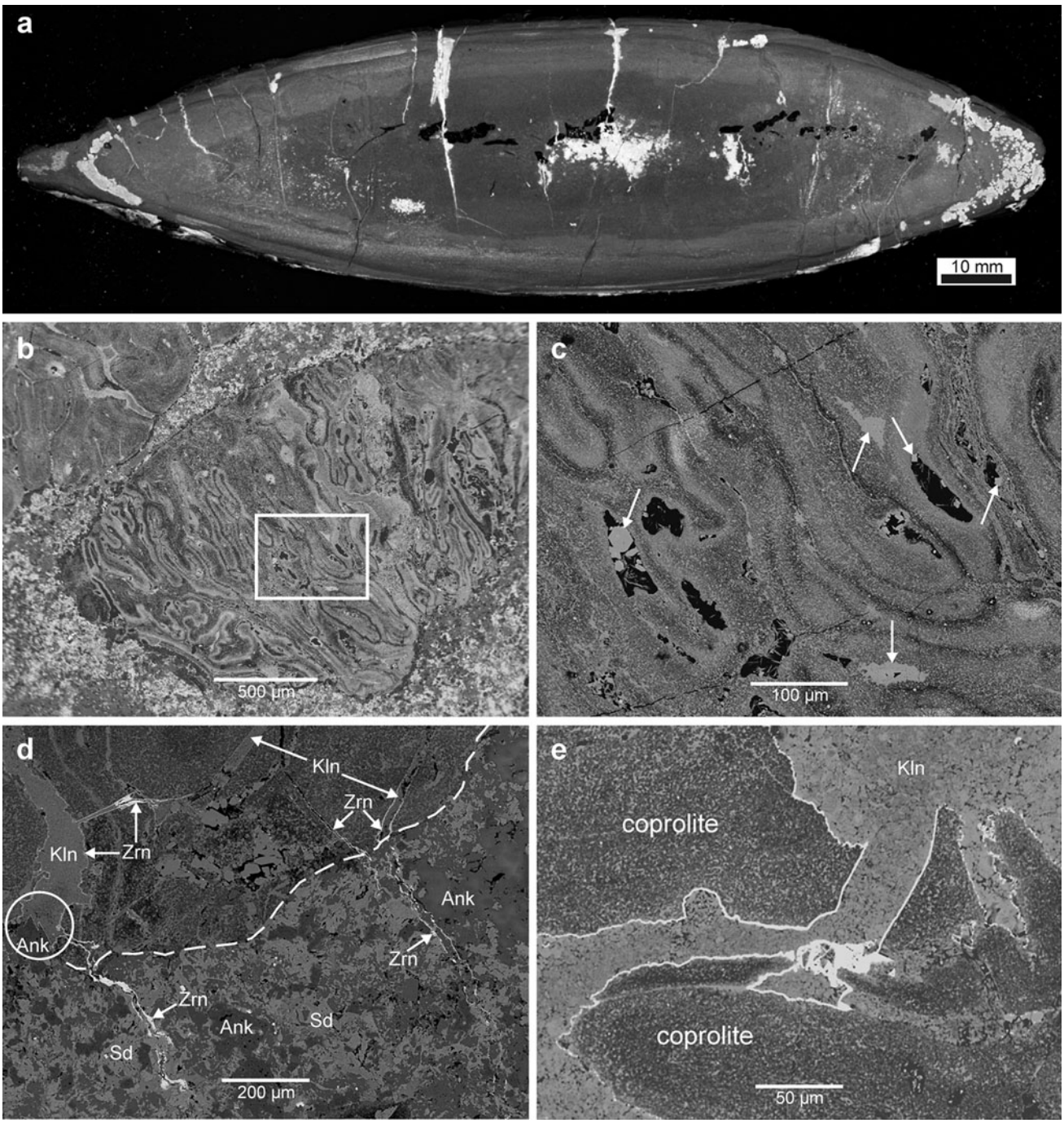


**Fig. 3** Zircon-bearing concretion *M*. **a** Cross-section revealing the internal structure with black coprolites, dark sideritic concretion body, and very bright pyrite dispersed in the concretion body, forming aggregates of filling cracks. **b** BSE image of a coprolite. Detail of the area marked in the *rectangle* is shown in **c**. **c** Detail of **b**. *Arrows* indicate authigenic apatite rich in F (chemical composition in the Supplementary Table 1). Some of them (on the *left*) are euhedral. **d**, **e** BSE images showing white zircon (Zrn) lining the crack walls cutting through phosphate coprolite. In **d,** the cracks cut through the coprolite (*top*) and propagate a little into the concretion body (*bottom*). The *dashed line* depicts the border between coprolite and concretion body. The concretion body consists of ankerite (Ank, *very dark gray*) and siderite (Sd, *light gray*) with minor calcite (*dark gray*). Kaolinite (Kln) fills the cracks within the coprolite, while ankerite, calcite, and siderite (the same as in the concretion body) fill the cracks beyond the coprolite. Morphology of the cracks indicates rather brittle deformation within the coprolites, while fluidal within the concretion body, where the cements seem to continue through the cracks. Zircon is earlier than kaolinite, but apparently later than ankerite (*encircled*)

**Table 1** Electron microprobe analyses of selected zircons from sample M

| Oxides | 1 | 2 | 3 | 4 | 5 | 6 | 7 | Elements | 1 | 2 | 3 | 4 | 5 | 6 | 7 |
|---|---|---|---|---|---|---|---|---|---|---|---|---|---|---|---|
| | wt. % | | | | | | | | Formulae based on 4 oxygens | | | | | | |
| $P_2O_5$ | 0.09 | 0.09 | 0.06 | 2.75 | 1.22 | 2.10 | 1.11 | P | 0.002 | 0.002 | 0.002 | 0.073 | 0.032 | 0.058 | 0.029 |
| $SiO_2$ | 31.86 | 32.07 | 31.65 | 28.56 | 30.57 | 29.07 | 30.33 | Si | 0.980 | 0.981 | 0.981 | 0.890 | 0.957 | 0.921 | 0.937 |
| $TiO_2$ | b.d. | b.d. | b.d. | 0.22 | 0.17 | 1.28 | 0.19 | Ti | 0.000 | 0.000 | 0.000 | 0.005 | 0.004 | 0.031 | 0.004 |
| $ZrO_2$ | 66.78 | 66.72 | 66.30 | 57.69 | 58.80 | 54.63 | 61.27 | Zr | 0.999 | 0.995 | 1.002 | 0.877 | 0.898 | 0.848 | 0.924 |
| $HfO_2$ | 1.29 | 1.23 | 1.48 | 0.41 | 0.41 | 0.39 | 0.39 | Hf | 0.011 | 0.011 | 0.013 | 0.004 | 0.004 | 0.004 | 0.003 |
| $Al_2O_3$ | b.d. | b.d. | b.d. | 0.59 | 0.93 | 1.98 | 0.79 | Al | 0.000 | 0.000 | 0.000 | 0.022 | 0.034 | 0.075 | 0.029 |
| $Y_2O_3$ | 0.08 | 0.08 | b.d. | 3.09 | 2.23 | 2.45 | 2.21 | Y | 0.002 | 0.001 | 0.000 | 0.051 | 0.037 | 0.042 | 0.036 |
| $Sc_2O_3$ | b.d. | b.d. | b.d. | b.d. | 0.36 | 0.34 | 0.32 | Sc | 0.000 | 0.000 | 0.000 | 0.000 | 0.009 | 0.009 | 0.009 |
| $La_2O_3$ | 0.04 | 0.04 | b.d. | b.d. | b.d. | b.d. | b.d. | La | 0.000 | 0.000 | 0.000 | 0.000 | 0.000 | 0.000 | 0.000 |
| $Ce_2O_3$ | b.d. | b.d. | b.d. | 0.03 | b.d. | b.d. | b.d. | Ce | 0.000 | 0.000 | 0.000 | 0.000 | 0.000 | 0.000 | 0.000 |
| $Nd_2O_3$ | b.d. | b.d. | 0.05 | b.d. | 0.09 | b.d. | 0.05 | Nd | 0.000 | 0.000 | 0.001 | 0.000 | 0.001 | 0.000 | 0.001 |
| $Gd_2O_3$ | b.d. | b.d. | b.d. | 0.04 | 0.06 | 0.07 | 0.06 | Gd | 0.000 | 0.000 | 0.000 | 0.000 | 0.001 | 0.001 | 0.001 |
| $Dy_2O_3$ | 0.22 | 0.22 | b.d. | 0.16 | 0.13 | 0.04 | 0.14 | Dy | 0.002 | 0.002 | 0.000 | 0.002 | 0.001 | 0.000 | 0.001 |
| $Ho_2O_3$ | b.d. | b.d. | 0.10 | b.d. | 0.13 | 0.16 | 0.10 | Ho | 0.000 | 0.000 | 0.001 | 0.000 | 0.001 | 0.002 | 0.001 |
| $Er_2O_3$ | 0.06 | 0.08 | b.d. | b.d. | 0.08 | 0.25 | 0.19 | Er | 0.000 | 0.001 | 0.000 | 0.000u | 0.001 | 0.003 | 0.002 |
| $Tm_2O_3$ | 0.10 | 0.10 | 0.03 | 0.03 | b.d. | b.d. | b.d. | Tm | 0.001 | 0.001 | 0.000 | 0.000 | 0.000 | 0.000 | 0.000 |
| $Yb_2O_3$ | 0.03 | 0.03 | b.d. | 0.29 | 0.20 | 0.27 | 0.16 | Yb | 0.000 | 0.000 | 0.000 | 0.003 | 0.002 | 0.003 | 0.002 |
| CaO | b.d. | b.d. | b.d. | 3.35 | 1.41 | 1.57 | 0.93 | Ca | 0.000 | 0.000 | 0.000 | 0.112 | 0.047 | 0.053 | 0.031 |
| FeO[b] | 0.32 | 0.32 | 0.04 | 1.22 | 0.47 | 1.70 | 1.43 | Fe | 0.008 | 0.008 | 0.001 | 0.032 | 0.012 | 0.045 | 0.037 |
| Total | 100.87 | 100.98 | 99.71 | 98.43[a] | 97.36[a] | 96.40[a] | 99.67[a] | Cations | 2.00 | 2.00 | 2.00 | 2.07[a] | 2.04[a] | 2.09[a] | 2.05[a] |

*b.d.* below detection

[a] Low totals and high cation sums caused by admixtures of other phases (see text)

[b] All Fe as FeO

## Zircon: composition, form, and structure

During SEM examination of certain concretions, very dense phases containing Zr and Si were found. They occur within voids and cracks in the phosphate coprolites (Figs. 3, 4, 5, 6; Supplementary Figures 2,3). The cracks are filled by later authigenic kaolinite and calcite. The chemical composition of these Zr-bearing phases, determined by electron microprobe, is given in Table 1. Measurements were made on the largest grains found in concretion M. Both the analytical totals and the cation totals point to satisfactory analyses and show that the phase is effectively end-member zircon (analyses no. 1–3). The analyses were performed on the spherical aggregates (no. 1–4) and bladed forms (no. 5–7). EMP analysis of the porous areas revealed, in addition to Zr and Si, the presence of Ca, P, Al, and Y, in proportions consistent with kaolinite, apatite, xenotime, and/or calcite. The phases were, however, too small for quantitative determination. A description of the three forms distinguished is given below. Analyses 4 through 7 have high concentrations of $Y_2O_3$ (2.2–3.1 wt. %) and HREE, which indicates the presence of a xenotime component. They also show elevated values of $SiO_2$, $Al_2O_3$, CaO, and $P_2O_5$. Since the analyzed grains are very small (up to 5 μm), it was difficult to perfectly focus the beam (diameter of ca. 2 μm) within them, the increased contents of the four elements come from the surrounding material. Excess of Si and Al comes from kaolinite, which fills the cracks, and Ca and P from amorphous Ca–phosphate, which is the main constituent of the coprolites. It is also significant that multiple microprobe analyses of the phosphatic coprolites revealed high contents of F, up to 4 wt. % (Supplementary Table 1). Concentrations of Pb, Th, and U have also been sought in the zircon, but were below detection limits.

The cracks within the coprolites are septarian in style, as they exhibit brittle deformation and do not propagate far into the body of the concretion, where they taper off abruptly (Fig. 3d). However, the zircon lining continues beyond the coprolites through the concretionary cements within confined narrow zones. These zones are prolongations of the cracks from the coprolites, but they exhibit fluidal characteristics (Fig. 3d). The observed relationships between authigenic phases indicate that zircon was formed after ankerite (Fig. 3d), synchronously with (Fig. 5b, d) and before calcite (Figs. 5a, c, 6b, c), and before kaolinite

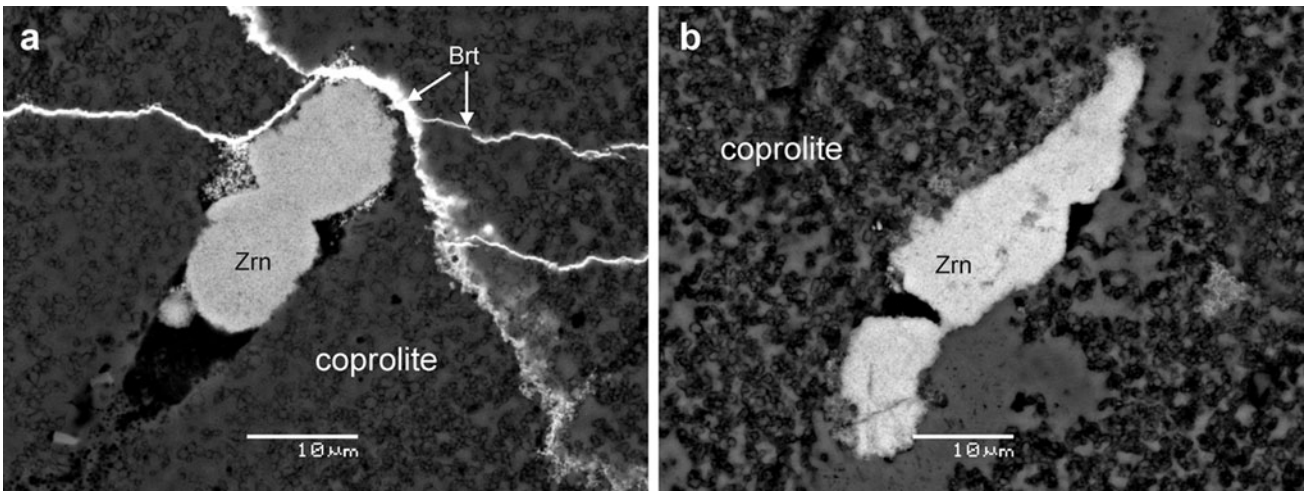


**Fig. 4** Scanning electron images (BSE) of zircon (Zrn) as porous grains filling voids in phosphate coprolite in sample M. White veins in **a** are barite (Brt)

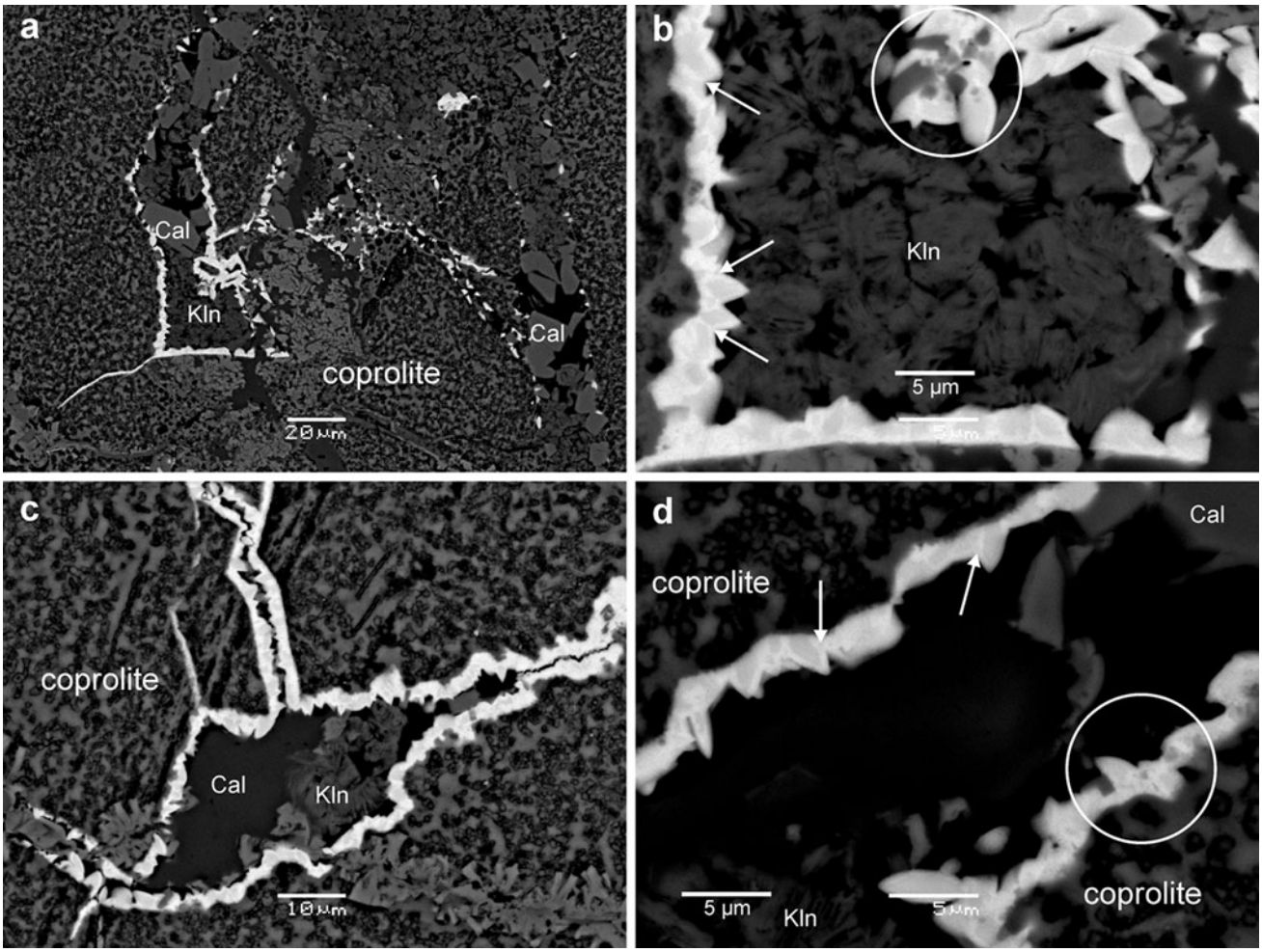


**Fig. 5** Scanning electron images (BSE) of euhedral zircon (*white*) with bladed habit lining crack walls in sample M. The inner parts of the cracks are filled with kaolinite (Kln) and calcite (Cal). Note zoning (*arrows*) of zircon crystals and intergrowths between zircon and calcite (*circles*) on **b** and **d**

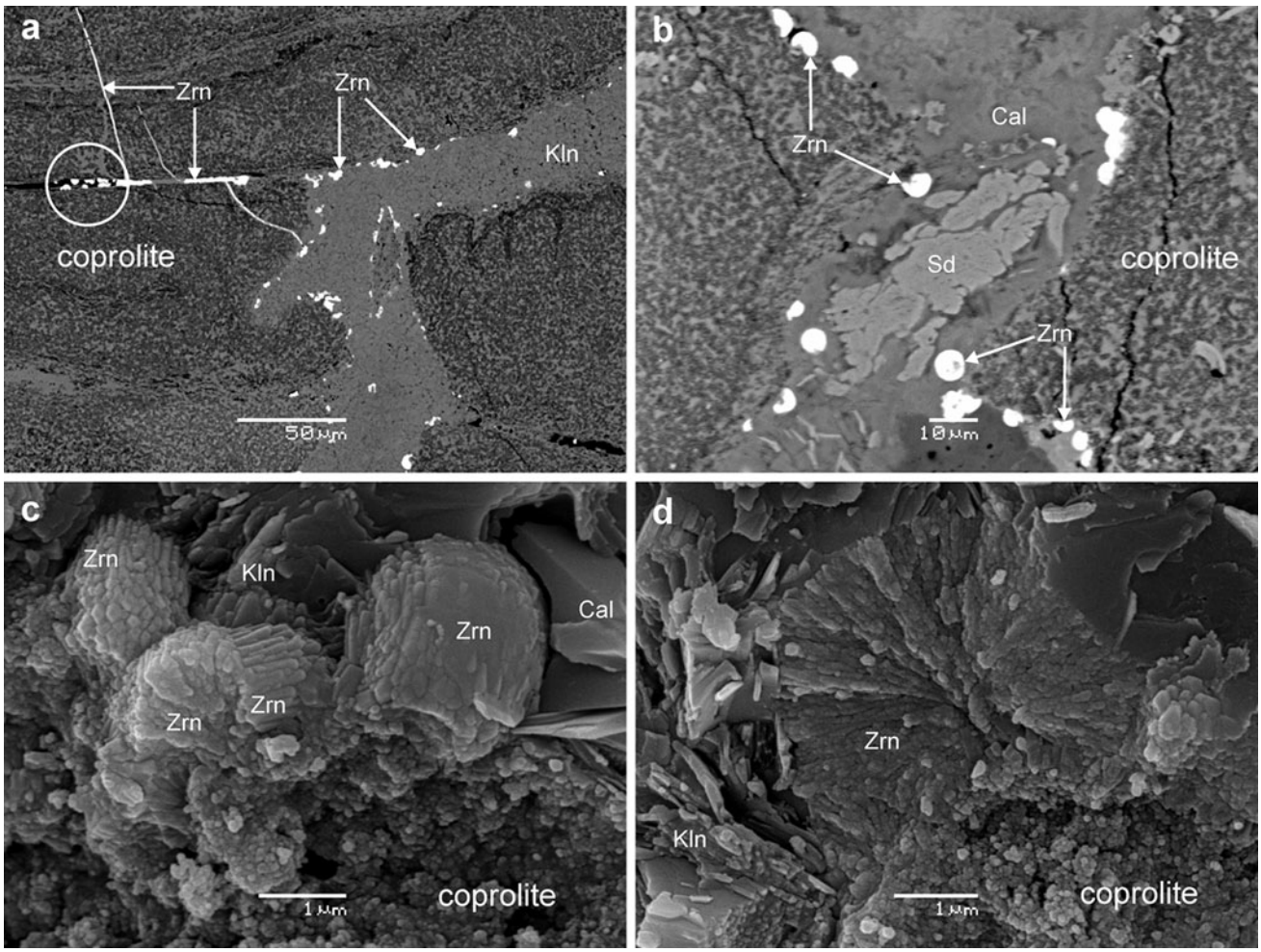


**Fig. 6** Scanning electron images of the spherical morphology of zircon (Zrn) in sample M. Cracks in the coprolite are filled with kaolinite (Kln), calcite (Cal), and siderite (Sd). **a**, **b** Images (BSE) of polished thin sections. In **a,** note the dense accumulation of spherical zircons, which produced a continuous infill of the crack (*encircled*). **c**, **d** Images (SE) of rock chips showing that the spherical zircons are in fact aggregates of prismatic individuals (**c**), sometimes in a radiating arrangement (**d**)

(Figs. 3d, e, 5, 6a, c, d) and late-diagenetic siderite (Fig. 6b).

More detailed and systematic observations with the SEM allowed us to distinguish three different types of zircon on the basis of morphology and microstructure. The first is porous zircon, which forms the largest grains (Fig. 4). The second is characterized by bladed, sawtooth-shaped, zoned crystals up to 5 µm long (Fig. 5). The form, microstructure, and emplacement imply that the crystals are not detrital and that they crystallized directly on the crack walls within existing concretions. The third morphology is spherical (Fig. 6a, b), which sometimes shows zoning (Supplementary Figure 2a, b) similar to that in the bladed grains. Where spherical zircon is abundant, it seems to form a homogenous, continuous blanket on the crack walls (Fig. 6a). SEM observation of rock chips revealed that the spherical forms are aggregates of prismatic individuals, sometimes in a radiating arrangement (Fig. 6c, d). Field emission electron microscopy was employed to examine the internal structure of these aggregates at the nanoscale. It revealed crystal faces of prisms and pyramids in tetragonal symmetry within the aggregates (Fig. 7). Although all three morphologies appear in the coprolites, they have not been observed together, so their time-dependent relationships are not known.

The outer zones (brighter in BSE) of the sawtooth-shaped and some spherical zircons are not due to electron charging, because they appear not only on the border between zircon and the surrounding phases, but also on the borders between adjacent zircon grains (Fig. 5b, d; Supplementary Figure 2). This and the aforementioned increased contents of Y and HREE in certain crystals (Table 1, analyses no. 4–7) are thought to be the result of

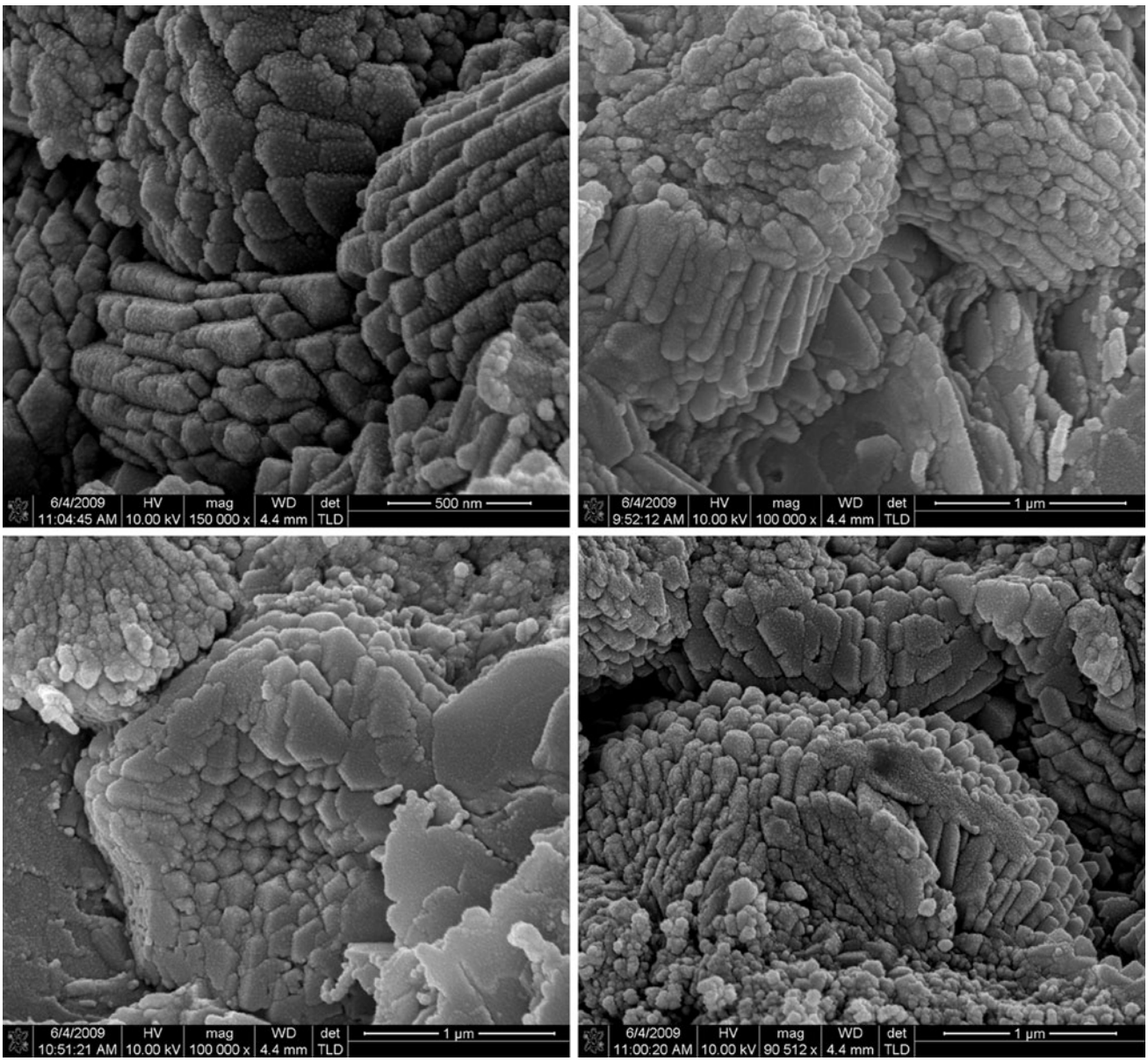


**Fig. 7** Field emission scanning electron images (SE) of the spherical aggregates of zircon in sample M. Note crystal faces of prisms and pyramids in tetragonal symmetry of individual prismatic crystals

chemical or even mineralogical variability, as these outer zones may be rich in a xenotime component.

## Inorganic geochemistry

Stable C and O isotope analyses were performed on the carbonate fraction of 14 concretions (36 samples; Table 2). Although 4 shale samples were also analyzed (As1, As2, Bs1, and Bs2), results were not obtained due to very low carbonate content. $\delta^{13}C$ and $\delta^{18}O$ values of the concretions range from −3.5 to 12.1‰ and from −12.8 to −4.7‰, respectively (Table 2). The results exhibit a positive correlation between $\delta^{13}C$ and $\delta^{18}O$ ($r^2 = 0.80$; Fig. 8). Multiple samples were collected from concretions A, B, E, and I along a vertical transect (Table 2; Fig. 8). The spread of $\delta^{13}C$ and $\delta^{18}O$ values in individual concretions can be as high as 14.4‰ (sample A) and 5.9‰ (sample B), respectively (Table 2).

Chemical analyses were made on three samples: concretion A (material from the concretion body without a coprolite), the adjacent shales collected from laminae laterally alongside (As1) and from beneath (As2) concretion A. As1 represents the sediments enveloped by concretion A. The sum of major elements derived from detrital

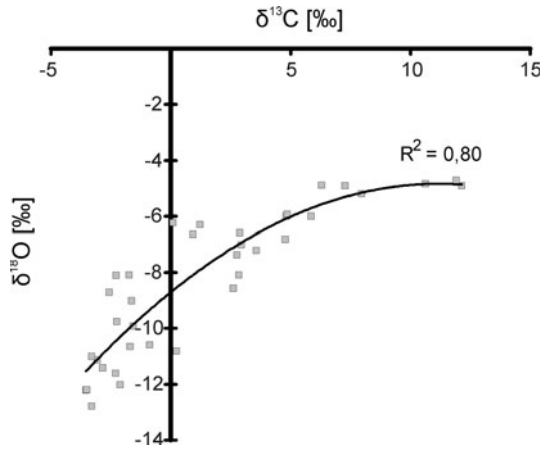


**Fig. 8** $\delta^{13}C$ versus $\delta^{18}O$ diagram of the carbonate fraction of 14 concretions (36 samples). *Black line* is the correlation line ($r^2 = 0.80$). Methanogenic source of bicarbonate is represented by the points at the *top right*, and the sulfate reduction source by points at the *bottom left*. For a detailed interpretation see the text

**Table 2** Stable C and O isotope composition of the concretions

| Sample | $\delta^{13}C$ [‰] | $\delta^{18}O$ [‰] | Sample | $\delta^{13}C$ [‰] | $\delta^{18}O$ [‰] |
|---|---|---|---|---|---|
| A1 | −2.3 | −8.1 | E3 | 0.9 | −6.6 |
| A2 | −1.7 | −8.1 | F | 1.2 | −6.3 |
| A3 | 2.8 | −7.4 | G | −3.3 | −11.0 |
| A4 | 5.9 | −6.0 | H | −3.5 | −12.2 |
| A5 | −2.2 | −9.8 | I1 | −1.6 | −9.0 |
| A6 | 12.1 | −4.9 | I2 | −2.8 | −11.4 |
| A7 | 11.9 | −4.7 | I3 | −1.6 | −9.9 |
| A8 | 10.6 | −4.8 | I4 | −2.1 | −12.0 |
| B1 | 2.8 | −8.1 | I5 | −1.7 | −10.6 |
| B2 | 4.8 | −6.0 | I6 | 3.6 | −7.2 |
| B3 | 7.3 | −4.9 | I7 | −3.1 | −11.1 |
| B4 | 8.0 | −5.2 | I8 | −2.6 | −8.7 |
| B5 | 0.2 | −10.8 | J | −2.3 | −11.6 |
| B6 | 4.8 | −6.8 | K | −0.9 | −10.6 |
| B7 | 2.6 | −8.6 | L | −3.3 | −12.8 |
| C | 4.9 | −5.9 | M | −3.5 | −12.2 |
| E1 | 0.1 | −6.2 | N | 3.0 | −7.0 |
| E2 | 2.9 | −6.6 | O | 6.3 | −4.9 |

material (Si + Al + Na + K + Ti + Cr) is more then 5 times higher in the shales than in the concretion (Supplementary Table 2). This approximates the relative dilution effect caused by the concretionary cements in the concretion. It is supported by the concentrations of trace elements typically bound to detrital material (Th, Zr), which are about 5 times higher in the shale As1 than in concretion A (Supplementary Table 2).

Five elements (Fe, Mg, Ca, Mn, and P) are significantly enriched in the concretion relative to the shales. Fe, Mg, Ca, and Mn are bound in the authigenic carbonates, which are the concretionary cements, while P comes from phosphate fish remains (Supplementary Table 2).

## Organic petrography and geochemistry

Vitrinite is common only in As2. In other samples, vitrinite grains were relatively infrequent, and in Bs1, they are also small in most cases. Average vitrinite reflectance values are shown in Table 3. The zircon-bearing concretion M and the surrounding shales Ms exhibit significantly higher vitrinite reflectance values (above 2.5 %) than the other two samples Bs1 and As2 (below 1.1 %). These values were calculated into approximate temperatures affecting the samples by application of Hunt's (1995) maturity parameters correlations. It showed that the rocks examined were influenced by diverse thermal regimes. The concretion M and the surrounding shales Ms recorded temperatures slightly above 200 °C, and the shales Bs1 and As2, temperatures below 100 °C (Table 3). The estimation by Hunt (1995) assumes that the peak temperature of vitrinite maturation depended on burial depth. However, if short-lived thermal processes, such as contact metamorphism or hydrothermal fluids migration, were the primary source of heat, the temperatures of vitrinite maturation might have been even higher (Barker and Lewan 1999, see also Stewart et al. 2005) than those calculated using Hunt's (1995) estimations, especially in the case of supercritical fluids migration (Barker and Lewan 1999). If the formula of Barker and Pawlewicz (1994) for hydrothermal regime is applied, the peak temperature for M and Ms samples would be around 70 °C higher than those calculated for burial regime (Table 3). Therefore, if the more mature samples M and Ms experienced hydrothermal heating, this would suggest that the vitrinite reflectance values indicate peak temperatures between 270 and 290 °C, which appears realistic for zircon crystallization.

Differences between analyzed samples were also obtained using aromatic molecular parameters based on methyldibenzothiophenes and methylphenanthrenes. The samples can be divided into two groups: A, As1, B, and Bs1 have lower and C and D higher values of the molecular parameters (Table 4). Authigenic zircon has been found in concretion D (Supplementary Figure 3). The calculated vitrinite reflectance values $R_{(DBT)}$ of methyldibenzothiophene ratio (MDR) are quite similar to those measured on vitrinite grains for mature and immature samples (compare Tables 3, 4). The difference in methylphenanthrene index (MPI1) between the two groups is smaller but still discernible.

Relatively low MPI1 values result from high concentrations of phenanthrene. Methylphenanthrene (MP) distribution in C and D with a strong preponderance of more stable 2- and 3-MP over 1-, 4-, and 9-MP (Fig. 9a) is

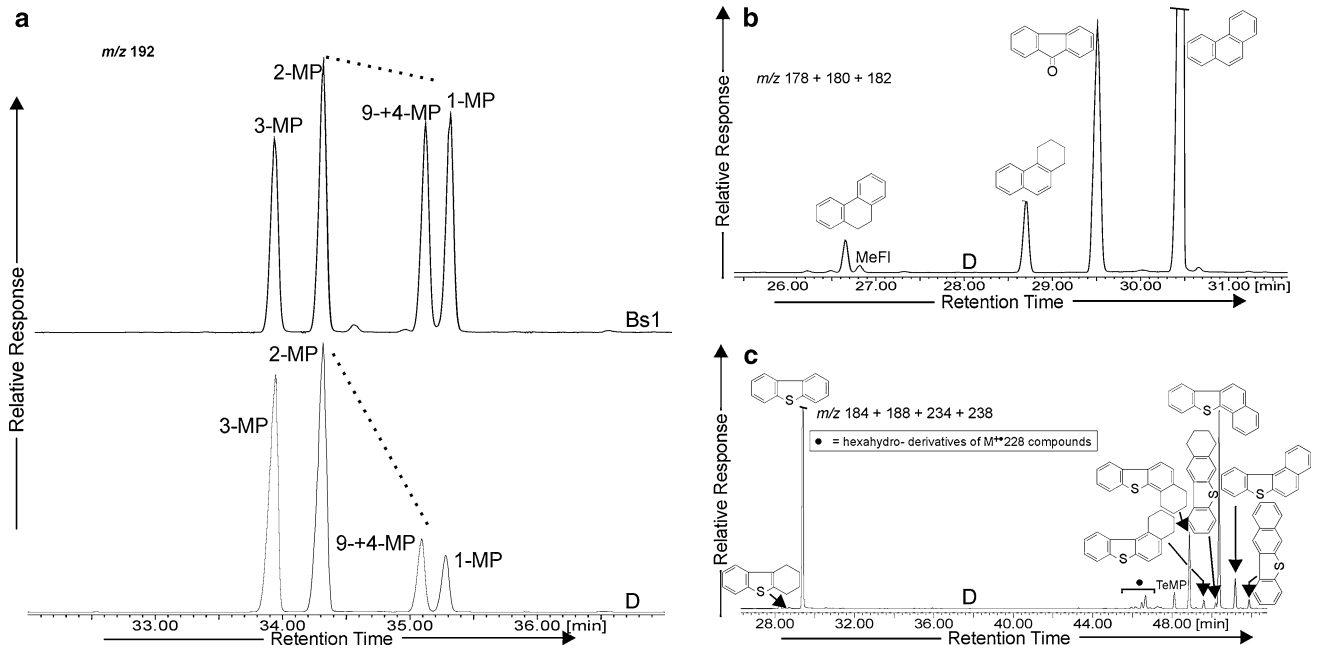


**Fig. 9** Partial and summed mass chromatograms for: **a** *m/z* 192, showing the different distributions of methylphenanthrenes caused by thermal maturity differences (Bs1 and D sample), **b** *m/z* 178 + 180 + 182, showing the distribution of phenanthrene, 9,10-dihydrophenanthrene, and 1,2,3,4-tetrahydrophenanthrene in sample D. *MFl* methylfluorene. **c** Summed mass chromatogram for *m/z* 184 + 188 + 234 + 238, showing the distribution of dibenzothiophene, 1,2,3,4-tetrahydrodibenzothiophene, benzo[*b*]naphthothiophenes, and their hydrogenated counterparts in the sample D. *TeMP* tetramethylphenanthrene isomer. DB-35MS column was used

**Table 3** Vitrinite reflectance measurements

| Sample | Vitrinite reflectance $VR_r$ [%] | | | | | $T_{burial}$ [°C][a] | $T_{hydrothermal}$ [°C][b] |
|---|---|---|---|---|---|---|---|
| | Avg value | SD | Min value | Max value | *n* | | |
| M concretion | 2.57 | 0.82 | 1.33 | 4.23 | 50 | ~200 | 273 |
| Ms shales | 2.83 | 0.96 | 1.32 | 4.42 | 30 | ~220–230 | 285 |
| Bs1 shales | 0.71 | 0.23 | 0.39 | 1.44 | 50 | ~70 | 108 |
| As2 shales | 1.09 | 0.24 | 0.52 | 1.76 | 100 | ~90 | 163 |

*Avg* average, *SD* standard deviation, *Min* minimum, *Max* maximum, *n* number of measurements

[a] estimated after Hunt (1995)

[b] estimated after Barker and Pawlewicz (1994): $T_{hydrothermal} = [\ln(VR_r) + 1.19]/0.00782$

typical of highly mature organic matter (Cassani et al. 1988; Szczerba and Rospondek 2010). In A, As1, B, and Bs1, such a distribution does not occur, but all isomers have similar relative concentrations (Fig. 9a).

It is especially interesting that highly mature samples contain di-, tetra-, and hexa-hydro-products of polycyclic aromatic hydrocarbons (PAHs). Tetrahexahydro-derivatives of PAHs including tetrahydronaphthalenes and tetrahydrochrysenes were recorded from the investigated area by George (1990), but without an interpretation of their source. We identified compounds that are di- and tetra-hydro-products of most of the aromatic compounds present in the samples, including phenanthrene (Fig. 9b), pyrene and fluoranthene, chrysene and triphenylene, as well as benzo[*a*]pyrene, benzo[*e*]pyrene, and isomers of benzofluoranthenes. Moreover, these samples contain tetrahydro counterparts of aromatic sulfur compounds like dibenzothiophene and benzo[*b*]naphthothiophenes (Fig. 9c), previously not reported from geological materials.

## Discussion

### Growth of the concretions and the timing/temperature of zircon formation

Five lines of evidence prove that the concretions are early-diagenetic features:

**Table 4** Molecular parameter values based on dibenzothiophene and phenanthrene distribution

| Sample | MDR | $R_{(DBT)}$ [%] | $T_{burial}$ [°C][a] | $T_{hydrothermal}$ [°C][b] | MPI1 |
|---|---|---|---|---|---|
| A concretion | 3.1 | 0.74 | ~80 | 114 | 0.56 |
| As1 shales | 3.3 | 0.75 | ~80 | 115 | 0.56 |
| B concretion | 1.5 | 0.62 | ~65 | 91 | 0.43 |
| Bs1 shales | 2.4 | 0.69 | ~70 | 105 | 0.46 |
| C coprolite | 22.9 | 2.18 | ~180 | 252 | 0.78 |
| D concretion | 27.3 | 2.50 | ~200 | 269 | 1.08 |

*MDR* 4-MDBT/1-MDBT (Radke et al. 1986)

$R_{(DBT)} = 0.51 + 0.073$MDR (Radke and Willsch 1994)

MPI1 = 1.5(2-MP + 3-MP)/(P + 1-MP + 9-MP) (Radke and Welte 1983)

[a] estimated after Hunt (1995)

[b] estimated after Barker and Pawlewicz (1994): $T_{hydrothermal} = [\ln(R_{DBT}) + 1.19]/0.00782$

1. The morphology of the concretions and the bending of shale laminae around them suggest that they were formed prior to mechanical compaction of the shales.
2. The concretions are so abundant in concretionary cements (estimated at up to 86 %) that the siliciclastic material is dispersed in isolated patches. This implies that the precipitation of carbonate cements was not just a passive infill of the available porespace but was displacive, which led to the dispersion of siliciclastic material. The sediments could not have been lithified before concretion formation in order to allow disruption of the detrital material by the displacive growth of cements.
3. The fact that fossils occur in each specimen suggests that the concretions grew due to the intensive decay of organic matter, which happens shortly after deposition.
4. The stable C isotope composition of some concretions is exceptionally heavy, with $\delta^{13}$C values above 5 and as high as 12.1‰, indicating methanogenesis as the main source of bicarbonate (Irwin et al. 1977; Raiswell 1987). Nevertheless, the range of $\delta^{13}$C values of all samples is large, from slightly negative to strongly positive. This proves that there was also a source of isotopically light bicarbonate, most probably liberated by oxidation of organic matter through sulfate reduction (Irwin et al. 1977; Raiswell 1987), although addition of bicarbonate from basin water is also possible. The $\delta^{13}$C values differ also within individual concretions, up to 14.4‰, which shows that bicarbonate from both sources (methanogenesis and sulfate reduction) was utilized in the precipitation of individual concretions. The diagenetic zone of methanogenesis spreads beneath that of sulfate reduction, which suggests that the concretions grew on the passage between those two shallow-diagenetic zones. The zone of sulfate reduction can occur immediately below the water/sediment interface down to several centimeters or tens of meters (Devol et al. 1984; Halbach et al. 2004), which supports precompactional, early-diagenetic formation of the concretions.
5. A positive correlation between $\delta^{13}$C and $\delta^{18}$O values implies that sulfate reduction–related pore waters were depleted in $^{18}$O relative to the methanogenesis-related pore waters. The degree of this depletion is too high (spread of $\delta^{18}$O values is 8.1‰, Table 2) to be exclusively temperature dependent, because it would mean that the temperature of the sulfate reduction–related fluids was around 60 °C, some 30 °C higher than those related to methanogenesis (based on the fractionation factor by Carothers et al. 1988). This is impossible, because the zone of methanogenesis occurs directly beneath that of sulfate reduction. Therefore, knowing that the sedimentary basin was brackish, we should expect a contribution of isotopically light meteoric water to the interstitial waters in the shallower sulfate reduction zone, which explains the gradual decrease in $\delta^{18}$O values towards the sulfate reduction–related pore water end-member. Because the shales are fine-grained and have low permeability, the possibility of percolation of the basin water confirms the very early-diagenetic formation of concretions in still unlithified sediments.

Zircon was found in the centers of the concretions, filling cracks, and voids within the coprolites. It crystallized after the formation of the concretion body, but synchronously with and before Fe-calcite, and before kaolinite, which are the latest phases filling the cracks. The cracks exhibit a septarian character, and they were presumably formed due to overpressure developed within the center of the concretion (see Hounslow 1997). Zircon occurs also within the concretion bodies surrounding the coprolites in fluidal-like narrow zones aligned with cracks from the coprolites. It is difficult to interpret the timing of zircon growth within

those zones. Textural relationships between zircon and concretionary cements may indicate that some portion of the carbonate cements postdates zircon growth. This would require zircon to grow at a similar temperature to the early-diagenetic carbonates, that is, way below 100 °C, which is not easy to envisage, although Hay and Dempster (2009) speculated that zircon crystallization may commence at temperatures as low as 100 °C. An alternative explanation is that the fluid containing dissolved Zr not only filled the cracks, but also injected the surrounding concretion body probably due to the pore fluid overpressure developed in the concretions during gradual burial (see Hounslow 1997).

Because the concretions and the shales do not show any petrographic evidence of metamorphism, zircon must have developed at a very low temperature. Growth of zircon at relatively low temperatures is well documented in the literature (Geisler et al. 2003; Rasmussen 2005; Hay and Dempster 2009; Hay et al. 2010), especially at temperatures above 250 °C under low-grade regional metamorphic conditions. We believe that this occurrence may be the first clear record of low-temperature zircon growth not as outgrowths, but as a separate crystalline precipitate in sedimentary rocks that do not show any petrographic indicators of metamorphism.

Organic geochemistry analyses were made in order to understand the thermal history of the study rocks. Vitrinite reflectance was measured in the zircon-bearing concretion M, in the shales surrounding the concretion Ms, and in two other shale samples. The results are dramatically different, which shows that it was not only burial that controlled the temperature. There must have been an additional, and spatially very restricted, heat source to heat up the organic matter in some samples to temperatures by more than 100 °C higher than in others from the same locality (Table 3).

The results of biomarker analysis also indicate very different degrees of thermal maturity between samples, which is shown by the distributions of methylphenanthrenes and methyldibenzothiophenes (Table 4). It is especially interesting that the highly mature samples contain di-, tetra-, and hexa-hydro-products of polycyclic aromatic hydrocarbons (PAHs) such as three- and four-ring phenanthrene (Fig. 9b), pyrene, fluoranthene, chrysene, triphenylene as well as five-ring PAHs like benzo[*a*]pyrene, benzo[*e*]pyrene, and isomers of benzofluoranthenes. Moreover, these samples contain the tetrahydro counterparts of aromatic sulfur compounds like dibenzothiophene and benzo[*b*] naphthothiophenes (Fig. 9c). Such products are not present in typical sedimentary organic matter and may only be formed under high-temperature aqueous conditions (McCollom et al. 1999). For example, large amounts of hydrogenated derivatives of phenanthrene and anthracene formed during a 3-day hydrous pyrolysis experiment at 330 °C (McCollom et al. 1999). These authors concluded that formation of these compounds requires chemical conditions that very rarely occur in nature (McCollom et al. 1999). The abundance of these compounds in highly mature samples suggests unique conditions where hydrothermal fluids played a crucial role.

All the data suggest that only some concretions were affected by hydrothermal activity, probably related to the shallow mafic intrusions that are common in the area, and it is in those concretions that authigenic zircon has been found. The hydrothermal activity caused the strong thermal maturation of organic matter. Later or at the same time, authigenic zircon precipitated in the cores of the highly mature concretions within voids developed in coprolites. We suggest, therefore, that the zircon formed by a dissolution–reprecipitation process. A similar process has been reported from the neighboring area of south-east Fife by Hay and Dempster (2009). They suggested that zircon alteration occurred below 100 °C on the basis of vitrinite reflectance measurements performed by Raymond and Murchison (1991) from Fife and Lothian. However, Hay and Dempster did not perform any geothermometric study of the samples they examined, using instead a regional estimate. Therefore, based on our interpretation of the Wardie data, we find it conceivable that the zircon alteration reported by them could have happened in a similar way, viz. by hydrothermal fluids at a higher temperature (~270 °C) than the regional maximal diagenetic temperature (60–90 °C). This is consistent with persistent magmatic activity in Fife throughout much of the Carboniferous (Read et al. 2002).

## Sources of substrates for zircon formation, growth mechanisms of zircon

Detrital zircon is a common accessory mineral in the shales from Wardie. It occurs mainly as rounded grains up to 30 μm without any unequivocal signs of dissolution, although some grains do exhibit complex outlines, possibly indicating corrosion (Fig. 2e–g). Thus, it is possible that some resorption occurred prior to the overgrowth of the unidentified phase. Detrital zircon is extremely rare or absent within the bodies of the concretions, despite careful search by SEM, although they contain the same siliciclastic material as the shales. We propose that zircon was dissolved from the body of the concretions, and maybe also from the shales, transported in fluids, and reprecipitated within voids in the phosphate coprolites. The fluids must have also dissolved the phosphate accessories, which have not yet been identified in the concretions. Evidence of their former presence may be found in those zircon grains which have a significant xenotime component.

The low-temperature dissolution of zircon requires specific conditions. Zr solubility can be enhanced by

radiation damage of the crystal lattice of zircon (Geisler et al. 2001), which causes weakening of the crystals and allows penetration by fluids (Hay and Dempster 2009). Zircon dissolution requires highly reactive fluids. Mobility of Zr in mudrocks can be significantly increased if a considerable amount of halogens, phosphate, or carbonate is liberated to the pore waters (Geisler et al. 2003; Rasmussen 2005). Although zircon is traditionally perceived as a refractory mineral, it is not necessarily the case in sedimentary environments. Zircon is particularly prone to metamictization, especially in fine-grained rocks dominated by reworked detrital material, and may suffer alteration and dissolution by fluids (Hay and Dempster 2009), especially hydrothermal fluids (Rubin et al. 1993; Geisler et al. 2003).

The concretions were preferentially formed around large coprolites and, therefore, in a phosphate-rich environment. The phosphates were remobilized at some stage, which released halogen- and phosphate-rich fluids, as shown by the presence of authigenic F-rich apatite (Fig. 3c, Supplementary Table 1). Carbonate was also dissolved in the fluids, as calcite is intergrown with authigenic zircon in the septarian cracks. Thus, we can speculate that detrital zircon was preferentially leached from the concretion bodies by these reactive halogen-, phosphate-, or carbonate-charged fluids and transported in solution to open spaces where it reprecipitated.

Microprobe analyses suggest also that, apart from Zr, considerable amounts of Y could have also been released during the hydrothermal processes, as considerable Y and P contents have been recorded in the sawtooth-shaped zircon with the brighter rims (Fig. 5, Table 1. point 1). We think that Y and P are present in these zircons as a solid solution towards xenotime, which is isostructural with zircon (Deer et al. 1997) or as exceptionally fine intergrowths between zircon and xenotime. Parageneses of authigenic zircon and xenotime overgrowths on detrital zircons have been reported by many authors (e.g. Rubin et al. 1993; Rasmussen 2005; Hay et al. 2010).

## Conclusions

Zircon is a very useful tool for dating and provenance studies, because it is normally stable in sedimentary environments. However, our finding shows that it is not always the case because conditions for dissolution and reprecipitation of zircon may exist in sedimentary rocks. Our finding may be unique and does not undermine the applicability of zircon studies in sedimentary material, but particular caution should be paid while studying samples from areas where hydrothermal activity has occurred. As a result of relatively high-temperature aqueous conditions related to hydrothermal fluids (~270 °C), perhaps associated with neighboring mafic intrusions, and the high concentrations of fluorine, phosphate, and carbonate in the fluids, the zircon was dissolved from the siderite concretions, transported in solution, and reprecipitated in voids. We can speculate that other accessory phases have formed in the same way but have been overlooked due to their very small size. They may be found during detailed study of relevant lithologies. Our work has extended the crystallization range of zircon to low temperatures and has documented its growth in sedimentary rocks, showing no petrographic indicators of metamorphism. Moreover, this is the first report on precipitation of authigenic zircon in sedimentary rock as a new phase, not as outgrowths. Such phases have the potential to allow chemical dating of the late stages of diagenesis, provided that in situ isotopic techniques with 1–2 μm spatial resolution can be developed (Rasmussen 2005) and that, unlike the zircons studied here, they contain measurable abundances of Pb, Th, and U.

**Acknowledgments** Funding for this research was provided by the Institute of Geochemistry, Mineralogy and Petrology, University of Warsaw. We thank Krzysztof Nejbert and Petras Jokubauskas for their help with sample preparation and SEM examination. We thank Harvey Belkin and Tim Dempster for detailed and constructive journal reviews.



## References

Barker CE, Lewan MD (1999) The effect of supercritical water on vitrinite reflectance as observed in contact metamorphism pyrolysis experiments. In: 27th national meeting, American chemical society, division of fuel chemistry, preprints of symposia 44(2):411–414

Barker CE, Pawlewicz MJ (1994) Calculation of vitrinite reflectance from thermal histories and peak temperatures. A comparison of methods. In: Mukhopadhyay PK, Dow WG (eds) Vitrinite reflectance as a maturity parameter: applications and limitations. ACS Symposium series 570, pp 216–229

Carothers WW, Adamia LH, Rosenbauer RJ (1988) Experimental oxygen isotope fractionation between siderite-water and phosphoric acid liberated $CO_2$-siderite. Geochim Cosmochim Acta 52:2445–2450

Cassani F, Gallango O, Talukdar S, Vallejos C, Ehrmann U (1988) Methylphenanthrene maturity index of marine source rock extracts and crude oils from the Maracaibo Basin. Org Geochem 13:73–80

Clarkson ENK (1986) Granton and Wardie shore. In: McAdam AD, Clarkson ENK (eds) Lothian geology; an excursion guide. Edinburgh Geological Society and Scottish Academic Press, Edinburgh, pp 1–221

Deer WA, Howie RA, Zussman J (1997) Rock forming minerals, vol 1A, Orthosilicates. The Geological Society, London, pp 1–919

Devol AH, Anderson JJ, Kuivila K, Murray JW (1984) A model for coupled sulfate reduction and methane oxidation in the sediments of Saanich Inlet. Geochim Cosmochim Acta 48:993–1004

Geisler T, Ulonska M, Schleicher H, Pidgeon RT, van Bronswijk W (2001) Leaching and differential recrystallization of metamict zircon under experimental hydrothermal conditions. Contrib Mineral Petrol 141:53–65

Geisler T, Zhang M, Salje EKH (2003) Low-temperature hydrothermal alteration of natural metamict zircons from the Eastern desert, Egypt. Mineral Mag 67:485–508

George SC (1990) The influence of igneous activity on the generation and accumulation of petroleum in the central area of the Midland Valley of Scotland. Unpublished Ph.D. thesis, University of Newcastle upon Tyne

George SC (1993) Black sandstones in the Midland Valley of Scotland: thermally metamorphosed hydrocarbon reservoirs? Trans R Soc Edinb Earth Sci 84:61–72

Halbach P, Holzbecher E, Reichel Th, Moche R (2004) Migration of the sulphate-methane reaction zone in marine sediments of the Sea of Marmara—can this mechanism be tectonically induced? Chem Geol 205:73–82

Hay DC, Dempster TJ (2009) Zircon alteration, formation and preservation in sandstones. Sedimentology 56:2175–2191

Hay DC, Dempster TJ, Lee MR, Brown DJ (2010) Anatomy of a low temperature zircon outgrowth. Contrib Mineral Petrol 159:81–92

Hounslow M (1997) Significance of localized pore pressure to the genesis of septarian nodules. Sedimentology 44:1133–1147

Hunt JM (1995) Petroleum geochemistry and geology, 2nd edn. Freeman WH, New York

Irwin H, Curtis C, Coleman M (1977) Isotopic evidence for source of diagenetic carbonates formed during burial of organic-rich sediments. Nature 269:209–213

Marynowski L, Kurkiewicz S, Rakociński M, Simoneit BRT (2011) Effects of weathering on organic matter: I. Changes in molecular composition of extractable organic compounds caused by paleoweathering of a Tournaisian marine black shale. Chem Geol 285:144–156

McCollom TM, Simoneit BRT, Shock EL (1999) Hydrous pyrolysis of polycyclic aromatic hydrocarbons and implications for the origin of PAH in hydrothermal petroleum. Energy Fuels 13:401–410

Radke M, Welte DH (1983) The methylphenanthrene index (MPI). A maturity parameter based on aromatic hydrocarbons. In: Bjorøy M et al (eds) Advances in organic geochemistry, 1981. Wiley, New York, pp 504–512

Radke M, Willsch H (1994) Extractable alkyldibenzothiophenes in Posidonia Shale (Toarcian) source rocks: relationship of yields to petroleum formation and expulsion. Geochim Cosmochim Acta 58:5223–5244

Radke M, Welte DH, Willsch H (1986) Maturity parameters based on aromatic hydrocarbons: influence of the organic matter type. In: Leythaeuser D, Rullkötter J (eds) Advances in organic geochemistry, 1985. Org Geochem 10:51–63

Raiswell R (1987) Non-steady state microbiological diagenesis and the origin of concretions and nodular limestones. In: Marshall JD (ed) Diagenesis of sedimentary sequences. Geol Soc Spec Publ 36:41–54

Rasmussen B (2005) Zircon growth in very low grade metasedimentary rocks: evidence for zirconium mobility at $\sim$ 250°C. Contrib Mineral Petrol 150:146–155

Raymond AC, Murchison DG (1991) Influence of exinitic macerals on the reflectance of vitrinite in carboniferous sediments of the Midland Valley of Scotland. Fuel 70:155–161

Read WA, Browne MAE, Stephenson D, Upton BGJ (2002) Carboniferous. In: Trewin NH (ed) The geology of Scotland, 4th edn. The Geological Society, London, pp 251–299

Rosenbaum J, Sheppard SM (1986) An isotopic study of siderites, dolomites and ankerites at high temperatures. Geochim Cosmochim Acta 50:1147–1150

Rubin JN, Henry CD, Price JG (1993) The mobility of zirconium and other "immobile" elements during hydrothermal alteration. Chem Geol 110:29–47

Stewart AK, Massey M, Padgett PL, Rimmer SM, Hower JC (2005) Influence of a basic intrusion on the vitrinite reflectance and chemistry of the Springfield (No. 5) coal, Harrisburg, Illinois. Int J Coal Geol 63:58–67

Sumner D (1991) Palaeobiology, taphonomy, and diagenesis of a Lower Carboniferous fish fauna. Unpublished Ph.D. thesis, University of St Andrews

Szczerba M, Rospondek MJ (2010) Controls on distributions of methylphenanthrenes in sedimentary rock extracts: critical evaluation of existing geochemical data from molecular modeling. Org Geochem 41:1297–1311

Traquair R (1877–1914) The ganoid fishes of the British Carboniferous formations. Part 1—Palaeoniscidae. Monogr Palaeontographical Soc 31:1–186

Wachter E, Hayes JM (1985) Exchange of oxygen isotopes in carbon-dioxide—phosphoric acid systems. Chem Geol 52:365–374

Wood SP (1975) Recent discoveries of Carboniferous fishes in Edinburgh. Scott J Geol 11:251–258